

INVESTIGATION OF CRYSTAL GEOMETRIES FOR FIBER COUPLED GAMMA IMAGING INTRA-OPERATIVE PROBES

Martin P. Tornai, *Student Member, IEEE*, Craig S. Levin, *Member, IEEE*, Lawrence R. MacDonald, *Student Member, IEEE*, and Edward J. Hoffman, *Senior Member, IEEE*

Division of Nuclear Medicine & Biophysics, Department of Molecular & Medical Pharmacology, UCLA School of Medicine, Los Angeles, CA 90095

ABSTRACT

CsI(Na), CsI(Tl) and NaI(Tl) scintillators coupled through optical fibers were investigated with simulations and measurements to evaluate their potential as gamma imaging intra-operative probes. Three coupling methods were employed: discrete crystals coupled one-to-one with the fibers; discrete crystals coupled through a light diffuser to an unmatched fiber array; and continuous crystals coupled directly to the fiber optic array. The discrete crystals were 4x4 element arrays ranging in size from 1x1x2.5 mm³ to 2x2x6 mm³. CsI(Na) produced the best pulse height and single crystal energy resolution (44% at 140 keV) when coupled through fibers to the photodetector. All elements of the arrays were completely resolved, indicating that the intrinsic spatial resolution will be determined by the crystal size. The spatial resolution for the 12.5 mm ϕ x 3.5 mm continuous crystals was ~1.33 mm FWHM. Preliminary imaging measurements faithfully reproduced the activity distributions and compared favorably with simulations.

I. INTRODUCTION

In many surgeries the detection of tumors and the identification of residual tumor is very difficult. As a partial solution to this problem, we are investigating small area intra-operative imaging detectors sensitive to the beta and gamma rays emitted from tumor seeking labeled radiopharmaceuticals. Complete resection of malignant cancers has been shown to increase the life span of patients at least a factor of two over partial resection [1], and in neurosurgery, it also improves the quality of life of the patient [2]. The problem in neurosurgery lies in the identification of the residual tumor, which is currently determined by the surgeons' judgment and histological samples, which can be taken and analyzed during the surgical procedure; but, this technique is time consuming and is frequently not performed [1].

One of the strengths of nuclear medicine techniques is the high tumor to background contrast possible with labeled tracers or monoclonal antibodies. For example, ²⁰¹Tl (~70 keV) and ^{99m}Tc-sestamibi (140 keV) have been shown to have 3.6 to 27.1 times greater uptake in malignant brain tumors than in healthy brain [3,4], and 6.1 times higher uptake in breast tumors than in normal fatty breast tissue [5]. The boundaries of the brain tumors are clearly identified with ^{99m}Tc-sestamibi [4], and the tumor boundary is the region that is most likely missed during surgery.

There is a growing body of literature on the use of non-imaging intra-operative probes for the location of otherwise undetectable radiolabeled tumor. Imaging devices constructed with somewhat larger dimensions than the non-imaging devices could aid in more accurate tumor localization due to: (1) the ability of an imaging device to sample a large area and still give good localization; (2) an imaging device can locate

the signal of the lesion in an area with background emissions; and (3) *in situ* imaging during surgery can immediately monitor successful removal of tumor.

We believe that the intra-operative imaging probes described here and in earlier work [6-10] form the basis of a new class of fiber-optically coupled imaging devices for use in surgery. Our use of thick scintillators offers higher gamma stopping efficiencies without the low energy spectral tailing observed in high Z, compound semiconductor imaging detectors of equivalent stopping thicknesses [11,12]. In addition, fiber-optic light guides insulate the operative cavity from all voltage and current sources while facilitating the miniaturization of the imaging device. In this work, we investigate gamma sensitive scintillation detectors of various geometries and their characteristics and performance for the proposed imaging task.

II. DETECTOR OPTIMIZATION

A. Detector Candidates

Several detector candidates were considered for use in the gamma imaging probe (Table 1). Important features of small scintillation detectors for likely clinical radiotracers (70-159 keV) include high efficiency for the gamma rays, good photofraction, and high light output. CsI(Na), with its relatively high stopping power for gammas, its high light output, and a peak wavelength well matched to the bialkali photomultiplier tube (PMT), is a top candidate. The relatively slow decay time of CsI(Na) would not cause problems since count rates of ~200 cts/sec/mm² are expected (as calculated from tracer studies in [13], analogous to tracers for potential use in this application).

While YSO has high light output and density, its effective Z is significantly lower than CsI(Na) which will compromise efficiency in very small crystals. GSO and LSO have high effective Z and densities, but GSO's light yield is too low, and

TABLE 1. Comparison of detector candidates for potential use in the intra-operative gamma imaging probe.

PROPERTY	SCINTILLATOR					
	YSO	GSO	LSO	NaI(Tl)	CsI(Tl)	CsI(Na)
Effective Z	34.2	58.6	65.5	50.6	54.1	54.1
ρ (gm/cm ³)	4.54	6.71	7.4	3.67	4.51	4.51
I (ph/MeV)	44k	9.5k	28k	38k	52k	39k
λ_{\max} (nm)	420	440	420	410	535	420
τ (nsec)	70	60	40	230	1000	630
Refraction n	1.8	1.91	1.82	1.85	1.80	1.84
Hygroscopic?	N	N	N	Y	Y	Y
Rugged?	Y	Y	Y	N	Y	Y

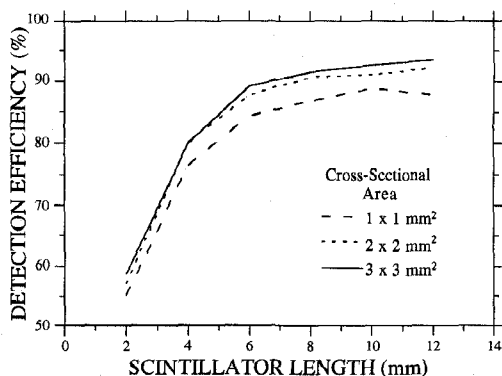


FIGURE 1. Monte Carlo results of detection efficiency of parallel-piped CsI scintillators for ^{57}Co gamma rays.

LSO is naturally radioactive and is inappropriate for a low count rate application. These properties make them unattractive for single photon imaging. CsI(Na) is less hygroscopic and has better stopping power than NaI(Tl), our initial first choice. Although CsI(Tl) has the highest light output and is otherwise almost identical to CsI(Na), its poor wavelength match to bialkali photocathode PMTs reduces its effective light output to $\sim 50\%$ of NaI(Tl).

B. Gamma Interactions and Optical Tracking

Gamma rays from a point source of ^{57}Co (122 keV 88%, 136 keV 12%) were simulated with a multiple interaction Monte Carlo code [14] to uniformly irradiate single parallel-piped CsI crystals ranging in size from $1 \times 1 \times 2 \text{ mm}^3$ to $3 \times 3 \times 12 \text{ mm}^3$. The simulations show that the dominant interaction at these energies is photoelectric, and that few of the gammas are scattered out of the crystal. There is only about a 6% loss due to scatter for the $1 \times 1 \times 6 \text{ mm}^3$ relative to the larger crystals (Fig. 1). The calculated gamma detection efficiency of CsI for near 140 keV gammas demonstrates that there is a greater dependence on the length of the scintillator than on the cross-sectional area (Fig. 1). This is consistent with other work on small scintillators [15,16]. These CsI results are consistent with an $\sim 35\%$ higher stopping power than NaI(Tl) crystals.

The detailed distribution of interactions from the Monte Carlo simulation were employed in optical tracking simulations using DETECT [17]. First, the results for the $2 \times 2 \times 6 \text{ mm}^3$ CsI scintillator were used to determine the effects of surface treatment on a parallel-piped scintillator coupled directly to a PMT. The simulation showed that the highest collection efficiency of scintillation photons (76% of photons generated) occurred when the distal surface from the PMT was roughened, and the sides of the scintillator were polished. These surface treatments promote total internal reflection along the side of the scintillator, while their direction of travel is somewhat randomized at the roughened surface with a cosine weighted bias, peaked in the direction of the PMT.

The optimal surface treatments were then utilized in the simulations for other sizes of scintillators. The optical photon tracking simulations demonstrate a dependence in both the length and cross-sectional area on light collection (Fig. 2). These results are also in general agreement with other work on light collection from small scintillators [15,16]. It should be noted that while the $1 \times 1 \text{ mm}^2$ curves in Fig. 2 are systematically lower than the other curves, the scale is expanded, and in comparing the photons detected for $1 \times 1 \text{ mm}^2$ and the 2×2

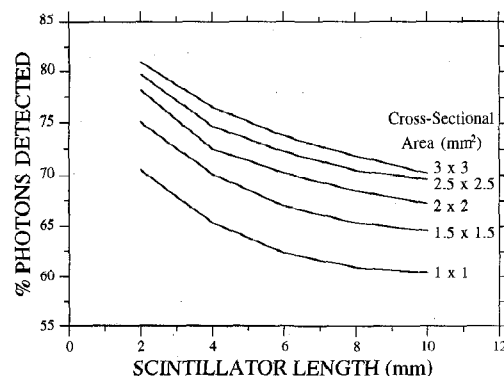


FIGURE 2. Dependence on length and cross-sectional area of photon collection in small parallel-piped scintillators.

mm^2 curves at 6 mm, for example, there is only an 11% difference.

III. IMAGING DETECTOR ARRAY COMPONENTS

A. Scintillation Detector Arrays

Discrete and continuous CsI crystal detectors ranging in size from $1 \times 1 \times 2.5 \text{ mm}^3$ to $2 \times 2 \times 6 \text{ mm}^3$ and $12.5 \text{ mm } \phi \times 3.5 \text{ mm}$ were evaluated for use in the fiber-optically coupled gamma imaging probe and compared with a discrete NaI(Tl) array (Table 2). The 4×4 element discrete detector arrays (Hilger Analytical) were cut from a single crystal of scintillator. The interdetector gaps (0.25 mm for the $1 \times 1 \text{ mm}^2$ and $1.5 \times 1.5 \text{ mm}^2$ element arrays, and 0.5 mm for the $2 \times 2 \text{ mm}^2$ element arrays) were filled with TiO_2 reflector doped epoxy. All arrays had $\leq 0.5 \text{ mm}$ thick layer of reflector on the gamma incident side of the crystals (distal to the photodetectors).

The thickness of the continuous crystals of CsI(Na) and CsI(Tl) (Advanced Detectors) ensured modest gamma detection efficiency at $\sim 140 \text{ keV}$ (3.5 mm corresponding to $\sim 79\%$ stopping efficiency for large detectors (cf. Fig. 1)) and warranted direct coupling to the optical fibers (Fig. 3, bottom). The addition of a light diffuser between scintillator and optical fibers, as in the beta probe case [9], would have degraded pulse height and energy resolution, as well as spatial resolution.

The sides of the cylindrical detectors were painted black to absorb reflections, which would otherwise lead to mispositioning errors [9]. The surface distal to the fibers for both continuous crystals was roughened and covered with several layers of Teflon tape, which has been shown to be an optimal surface treatment for good spatial and energy response [9,18].

Pulse height and energy resolution measurements were made with the continuous crystals and the arrays on a single channel PMT (RCA 4900), since no direct coupling to the multi-channel PMT (see III.C.) could be made. These direct coupled measurements were compared with measurements through the fiber optic imaging bundle (next section) coupled to the single channel PMT. Collimated sources (^{241}Am , 59 keV; ^{57}Co ; ^{137}Cs , 663 keV) irradiated the centers of the continuous crystals and an inner crystal in the 4×4 arrays.

B. Front-End Fiber Optics

Three methods of coupling the detector arrays to the front-end fiber optic bundles of the imaging probe were evaluated (Fig. 3). These included: (1) direct one-to-one crystal-optical fiber coupling; (2) coupling the discrete crystals to the front-

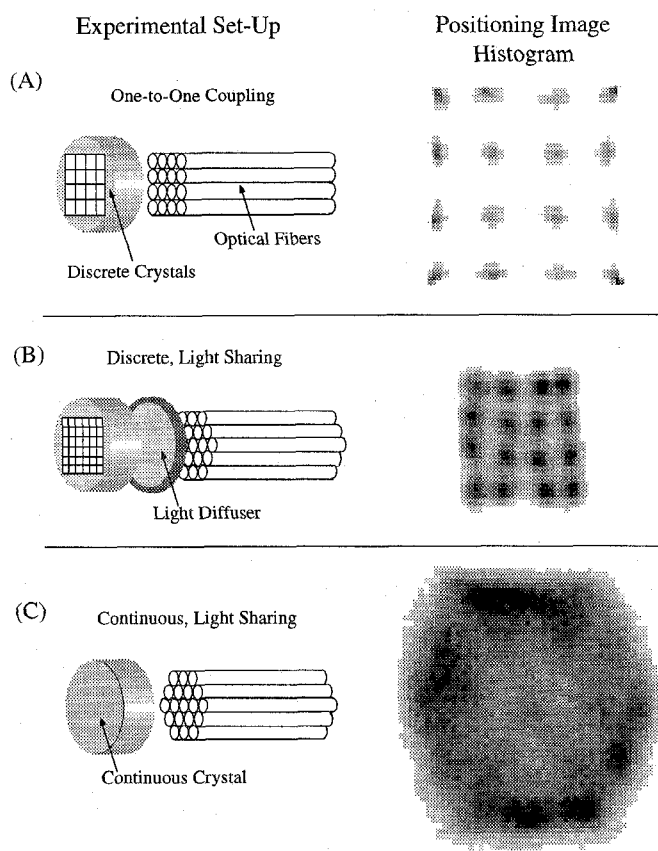


FIGURE 3. Comparison of the experimental coupling between (A) $1 \times 1 \text{ mm}^2$ CsI(Tl) discrete detectors and one-to-one coupled fibers, (B) $1 \times 1 \text{ mm}^2$ CsI(Tl) discrete detectors with light sharing coupling to fibers (NB: one-to-one coupling is not necessary), and (C) $12.5 \text{ mm } \phi$ CsI(Na) continuous crystal detector coupled with intrinsic light sharing to optical fibers.

end fiber optic array through a light diffuser (discrete, light sharing case); and (3) coupling the continuous crystals directly to the front-end fiber optic array (continuous, light sharing case). Each case was characterized in terms of energy resolution, efficiency, and spatial resolution.

For the one-to-one coupling scheme, the $1 \times 1 \text{ mm}^2$ and $2 \times 2 \text{ mm}^2$ detectors were coupled to 0.925 mm and 2 mm diameter (ϕ), double clad optical fibers (Numerical Aperture (NA) = 0.72; Kuraray International), respectively, arranged with the same pitch as the 4×4 element scintillator arrays. The 10 cm long optical fibers were embedded in white plastic which acted as a physical support for the fibers, and as part of the reflector surface of the crystal. This was important for the $1 \times 1 \text{ mm}^2$ crystals, since approximately 30% of the surface was not coupled to the optical fibers.

The hexagonal arrangement of 19 - 2 mm ϕ double clad optical fibers used in the beta imaging probe [7,9] and preliminary work on the gamma imaging probe [10] was employed for the discrete, light sharing case. In essence, this design provides an image of the light from the detector array, similar in principle to PET block detectors [19,20]. In the image, the region corresponding to an individual crystal can be determined and that information is used in subsequent imaging measurements. In order to produce a useful image of a square detector array, a light diffuser is placed between the scintillators and optical fibers. The optimal thickness of the diffuser was deter-

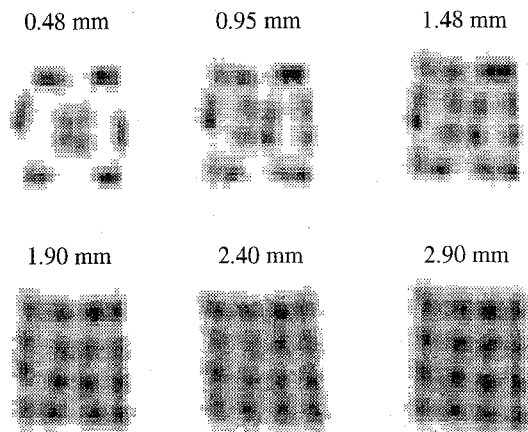


FIGURE 4. Effect of the light diffuser between the $1 \times 1 \times 4 \text{ mm}^3$ element CsI(Tl) crystal array and front-end optical fibers.

mined using the $1 \times 1 \times 4 \text{ mm}^3$ element CsI(Tl) array with a variety of diffusers (Fig. 4). The plastic (PMMA, $n = 1.49$) light diffuser thicknesses ranged from 0.48 mm to 2.9 mm. Each diffuser had highly polished faces and roughened sides painted with black absorber. The best compromise of detector pulse height, resolution of the elements, and sensitivity uniformity was reached with a 1.9 mm thick diffuser. The pulse height degraded ~21% in amplitude when the 1.9 mm light diffuser was used compared to no light diffuser. However, the best energy resolution values were obtained with this thickness. Optical fibers with a different NA would most likely require a different diffuser thickness. The use of another light diffuser (e.g. polystyrene) could also affect the thickness, due to the different refractive index of the material.

The continuous crystal light sharing case is similar to the continuous crystal beta imaging intra-operative probe [7-9]. Previous simulations and measurements demonstrated that thicker continuous scintillators coupled to fiber optics have poorer spatial resolution [9,21] due to light spread within the scintillator volume. There are also variations in pulse height response due to depth of interaction in these continuous crystals [21]. There were no light diffusers used with the continuous crystals as the crystals provided a sufficient area to thickness ratio to expect reasonable spatial resolution. Spatial resolution with continuous crystals coupled to optical fiber detectors is governed by Poisson statistics, with additional limiting effects due to the NA of the optical fiber. That is, the optical fiber limits the acceptance cone for light from the scintillator [9] introducing second order effects on the resolution.

C. Photodetector and Electronics

The Philips XP1722 multi-channel PMT (MC-PMT) was used as the photon detector for the array evaluations and imaging measurements. This MC-PMT was found to have good characteristics for fiber coupled imaging detectors in earlier work [9]. The fiber optics (16 square grid or 19 hexagonally arranged fibers) are coupled to individual detector channels and the parallel outputs feed two distinct resistive charge division networks. The charge division networks result in four outputs representing signals from the +X, -X, +Y and -Y directions. Each output signal has an i -V converter/line driver with 2 μsec shaping, impedance matched to the NIM shaping and discrim-

inating electronics. The resultant signals are then digitized in list mode with CAMAC BiRa ADCs and further processed to form an image with the standard Anger ratio equations, similar to the beta imaging probe. The shaping time of 2 μ sec gave the best energy resolution for both the CsI(Tl) and CsI(Na) scintillators. Data acquisition control with LabVIEW™, and image processing and display was on a Macintosh IIfx computer. All data were collected in list mode to allow retrospective definition of data collection parameters and data analysis.

The charge division network for the hexagonal arrangement has independent gain balancing for each channel [9]. This is necessary to ensure uniform amplitude of the shared light signals for a given energy deposition. This is similar in principle to the PMT gain balancing necessary on standard Nuclear Medicine gamma cameras [22]. The charge division network for the square grid arranged fibers is a different network with no gain balancing of the independent signals. The optical signals from the discrete one-to-one coupled scintillator and fiber optic are not shared. Hence, the optical signal in any fiber is independent of signals in other fibers, and it is not necessary to normalize the signals to get the correct position. The event positions are completely determined by the values from the charge division circuit [23].

IV. DETECTOR PERFORMANCE

A. Flood Field Responses

All of the detector arrays and configurations were irradiated with ^{57}Co gammas ($\tau_{1/2} = 217\text{d}$; 122 keV 88%, 136 keV 12%). These gamma ray energies are near 140 keV, which is the energy of gamma rays emitted from $^{99\text{m}}\text{Tc}$ ($\tau_{1/2} = 6.01\text{h}$) labeled radiopharmaceuticals anticipated for use with the imaging probe.

For the one-to-one crystal-to-fiber coupling scheme, the flood field histograms of the various detector sizes were similar (Fig. 3, top). While up to 8x8 scintillator array elements have been read out with this charge division technique [23], the number of detectable elements is limited by the number of photodetectors. The primary advantage of this technique, however, is that there is minimal cross-talk between detector elements, for even very low light levels. In addition, gain balancing is not necessary because the positioning uniformity is not dependent on a shared optical signal. The distributions are somewhat distorted, however, because of the positioning errors with charge division due to low photon statistics, and also the series and parallel noise contribution in the circuit from the resistive charge division itself. Capacitive division has demonstrated lower noise characteristics [24] and may be even better for charge division networks with MC-PMTs.

The flood field responses of 3 detector arrays employing light sharing positioning are shown to completely resolve even the smallest, 1x1 mm² crystal elements (Fig. 5). The 1.9 mm thick light diffuser was used in all three cases. Because the 4x4 element arrays of 2x2 mm² detectors were too large to be completely viewed by the optical fiber bundle, the arrays were masked off to 3x3 elements. Imaging with these discrete light shared arrays requires that the optical fiber channels and associated photodetectors are gain balanced so that the resultant image histogram of the scintillation detectors is undistorted and uniform in detector location and count density. Images of the type seen in Fig. 5 are basically a mapping of the X and Y signal from the imaging systems and can be used

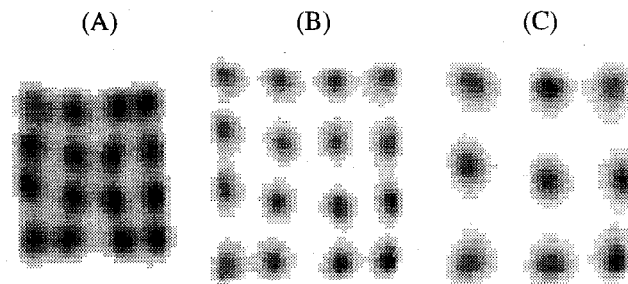


FIGURE 5. Flood field responses with ^{57}Co irradiation of the (A) 4x4 element 1x1x4 mm³ CsI(Tl), (B) 4x4 element 1.5x1.5x6 mm³ CsI(Na) and (C) 4x4 element (masked to 3x3 to fit onto the fiber optic FOV) 2x2x4 mm³ CsI(Tl) arrays coupled with light sharing to the hexagonal optical fiber bundle. Each image is a subset of a 64x64 pixel image positioning histogram.

to define the region that corresponds to each crystal. This is used to create a corresponding look-up matrix that uses the X and Y values as an address and returns the crystal number upon being accessed [10].

The continuous crystals were similarly flood irradiated (Fig. 3, bottom). This detector configuration is the most like standard gamma camera systems. The energy and pulse height responses of this configuration depend on having good uniformity for the detectors (optical fiber and photodetectors) and thus gain balancing for each optical fiber channel is necessary.

B. Energy Resolution and Pulse Height

A summary of the results of flood irradiation of the imaging detector arrays is presented in Table 2. Because of its better spectral match to the alkali MC-PMT photocathode, the signal from CsI(Na) was significantly higher in amplitude than CsI(Tl) (Table 2 and Fig. 6). One reason for the relatively modest energy resolution improvement of CsI(Na) over CsI(Tl) is the depth dependence of the number of photons reaching the photocathode in a narrow scintillator. Although the average number of scintillation photons has increased by a factor of about two, those gammas that interact at the face of the crystal will produce fewer photoelectrons than those interacting near the PMT. Another reason is the limitation imposed by the optical fibers. This effect causes an intrinsic broadening of the photopeak.

The FWHM energy resolutions at 122 keV for the CsI(Tl) and CsI(Na) continuous crystals were 25.8% and 24.1%, respectively, with the detectors directly coupled to the single channel PMT. The pulse heights were attenuated a factor of ~6 with the addition of the fibers between the crystals and PMT, which corresponded to the observed loss in resolution.

With the single channel PMT configuration, the resolutions of an element in the NaI(Tl) array, 2x2x4 mm³ element CsI(Tl) array, and CsI(Na) array were 18.2%, 19.5%, and 19.8%, respectively. There was only a factor of ~3 attenuation with the addition of the fiber optics and light diffusers between the scintillators and PMT, which corresponded to the observed loss in resolution. When a 3 mm PMMA light diffuser, analogous to the hermetic glass seal on the NaI(Tl) array, was placed directly between the 2x2x4 mm³ element CsI(Tl) array and PMT, the pulse height was attenuated by 71%, along with an energy resolution degradation to 29.7% FWHM. Note however, that for the results with the imaging detector with discrete, light sharing (Table 2), the NaI(Tl) array

TABLE 2. Summary of various detector array elements' characteristics with ^{57}Co irradiation measured through the optical fibers.

COUPLING / DETECTOR (mm^3)	% FWHM* (at 122 keV)	REL. PULSE HEIGHT*	EFF. $\pm\sigma$ (%) [†]
<i>One-to-One Coupling</i>			
NaI(Tl) 2x2x6	61.7 \pm 7.3%	59 \pm 18%	9.7
CsI(Tl) 1x1x2.5	63.3 \pm 7.5%	49 \pm 16%	5.8
CsI(Tl) 1x1x4	67.4 \pm 8.3%	38 \pm 16%	6.8
CsI(Tl) 2x2x4	57.8 \pm 6.6%	49 \pm 17%	4.0
<i>Discrete, Light Sharing Coupling</i>			
NaI(Tl) 2x2x6	60.4 \pm 4.3%	72 \pm 21%	4.7
CsI(Tl) 1x1x2.5	57.6 \pm 3.0%	56 \pm 8%	11.7
CsI(Tl) 1x1x4	57.4 \pm 3.9%	47 \pm 8%	13.4
CsI(Tl) 2x2x4	55.8 \pm 5.3%	53 \pm 12%	2.1
CsI(Na) 1.5x1.5x6	51.8 \pm 5.1%	100 \pm 14%	12.7
<i>Continuous, Light Sharing Coupling</i>			
CsI(Tl) 12.5 ϕ x 3.5	-	18	19.1
CsI(Na) 12.5 ϕ x 3.5	70.6	67	19.0

*Errors are the % standard deviations (SD) of the measured values for all the elements in the various detector arrays.

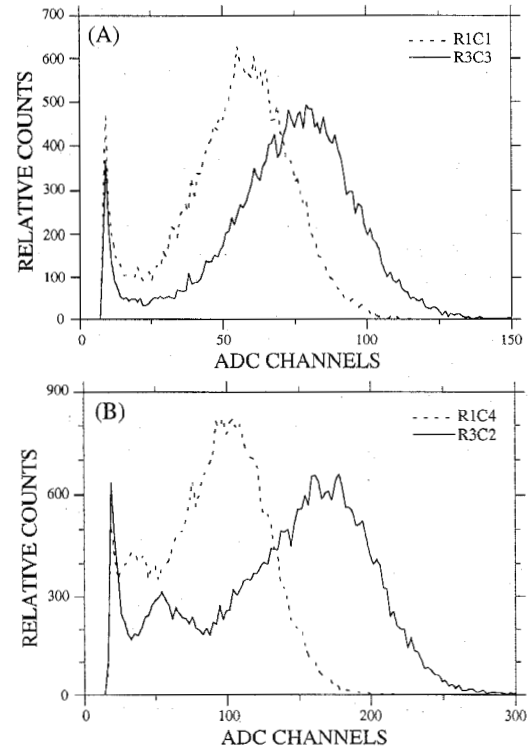
[†]Defined as the \pm SD of the integrated photopeak counts for each detector element. For the continuous crystals, defined in 75% of the image FOV.

measurements did not use any additional light diffuser, in contrast to all the CsI array measurements.

In another set of experiments, ^{57}Co and ^{137}Cs irradiated the CsI(Na) array and continuous crystal, either directly on the PMT or through the optical fibers. The relative statistical improvements at the different energies were identical ($\pm 2\%$) for pulse height and energy resolution when the detectors were in direct contact with the PMT. However, for both scintillators through the fibers, the relative energy resolution improvements corresponded to only $\sim 65\%$ of the improvements observed in pulse height. These preceding single channel PMT measurements corroborate the assertion of an intrinsic rather than statistical broadening of the photopeak most likely due to the effects of the optical fibers and various light guiding components.

Measured with the single channel PMT, the pulse height of the directly coupled 12.5 mm ϕ CsI(Na) crystal was 28% higher than the directly coupled 1.5 x 1.5 mm² CsI(Na) crystal. However, loss of light when the crystals were coupled with optical fibers caused the pulse height of the continuous crystal to be 33% less than the discrete crystal. These losses in the optical fiber are consistent with the measured imaging detector results in Table 2 and with previous reports [16,18].

An unexpected result was that the pulse heights from the light shared configurations were essentially equal to the directly coupled configurations (Table 2). The poor pulse height for the NaI(Tl) array can be attributed to the 3 mm thick glass plate providing a hermetic seal for the crystal, but also causing excess diffusion of the scintillation photons for non-optimal light transfer and collection. The light sharing coupled continuous detectors had the poorest overall performance. The scintillation light generated within the detectors is distributed among all the optical fiber elements, thus each optical fiber collects a relatively small fraction of the total light generated. Additional losses due to the optically absorptive sides also affect the pulse height and energy resolution of

**FIGURE 6.** Comparison of the measured highest and lowest pulse height responses at 122 keV from the (A) 1x1x4 mm³ CsI(Tl) and (B) 1.5x1.5x6 mm³ CsI(Na) arrays. Legends indicate Row and Column for elements in Fig. 5.

the continuous detectors.

The position of crystals within the array also affects the spectral characteristics of the signal in the light shared configurations (Figs. 7 and 8). The energy resolution was better for elements towards the center of the detector arrays. A similar effect has been observed in pseudo-discretized PET block detectors [25]. The effect is most likely due to the fact that the central crystals can share light among the fibers that surround its position, and edge crystals have no fibers to one side. For continuous imaging detectors, this effect is manifested as a non-linearity at the edge of the photodetector array due to the lack of elements beyond the edge photodetectors [26].

C. Efficiency Variations

Energy windows were retrospectively set on photopeaks on list mode data to determine the efficiency of each crystal. The integrated counts in these windows represent the relative efficiencies of each crystal. Variation in efficiency was small (right col., Table 2) but improvements to minimize the variations are warranted to match NEMA acceptance criteria for standard gamma cameras. Efficiency variations were less position dependent than pulse height and energy resolution (cf. Figs. 7 and 8). Efficiency maps for discrete crystal arrays, after electronic windowing and conversion to the look-up tables, are used as correction maps for spatial resolution and imaging measurements. Continuous crystal measurements used high statistics flood field images as the correction maps.

D. Line Spread Function Responses

The spatial resolution was measured for a number of the light sharing imaging arrays by stepping a 0.3 mm Pb slit

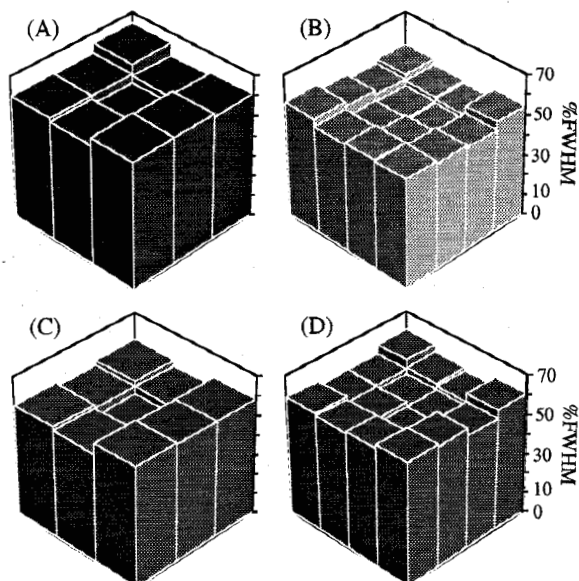


FIGURE 7. Comparison of the % FWHM energy resolution variations at 122 keV for the (A) $2 \times 2 \times 6$ mm³ element NaI(Tl) array, (B) $1.5 \times 1.5 \times 6$ mm³ element CsI(Na) array, (C) $2 \times 2 \times 4$ mm³ element CsI(Tl) array, and (D) $1 \times 1 \times 4$ mm³ element CsI(Tl) array.

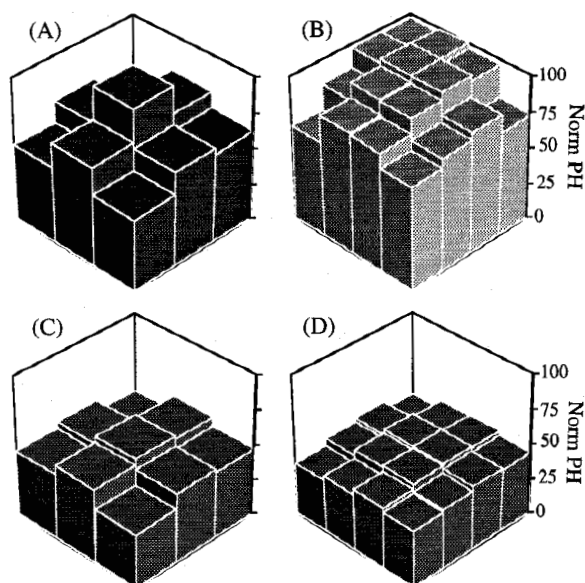


FIGURE 8. Comparison of the 122 keV photopeak pulse height variations for the (A) $2 \times 2 \times 6$ mm³ element NaI(Tl) array, (B) $1.5 \times 1.5 \times 6$ mm³ element CsI(Na) array, (C) $2 \times 2 \times 4$ mm³ element CsI(Tl) array, and (D) $1 \times 1 \times 4$ mm³ element CsI(Tl) array.

collimator and ⁵⁷Co source in 0.2 mm increments across the faces of the arrays. The FWHM of the resultant line spread function (LSF) profiles was then determined from the data plotted in Figs. 9A and 9B. The slit source was stepped in 1.0 mm increments for the continuous crystals and the LSFs fit with Gaussians (Figs. 9C and 9D). With a low energy threshold and efficiency normalized data, the mean LSFs were 0.92 ± 0.03 mm, and 1.21 ± 0.07 mm FWHM for the $1 \times 1 \times 4$ mm³ CsI(Tl) and $1.5 \times 1.5 \times 6$ mm³ CsI(Na) arrays, respectively. For the crystal arrays, the spatial resolution roughly corres-

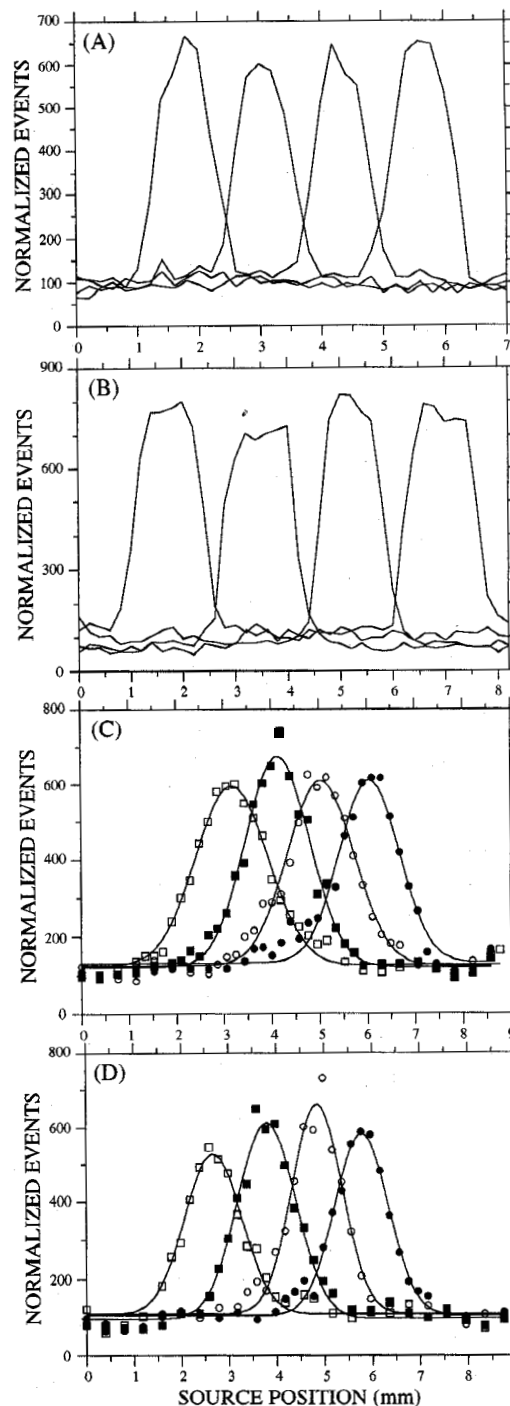


FIGURE 9. Efficiency normalized LSF responses for the (A) $1 \times 1 \times 4$ mm³ CsI(Tl) array, (B) $1.5 \times 1.5 \times 6$ mm³ CsI(Na) array, and the (C) $12.5 \phi \times 3.5$ mm³ CsI(Tl) and (D) $12.5 \phi \times 3.5$ mm³ CsI(Na) continuous crystals with Gaussian fits to the data.

ponded to the crystal size.

The resolutions of the continuous crystals varied as a function of light output of the scintillator. The $12.5 \phi \times 3.5$ mm³ continuous CsI(Tl) crystal had a 1.59 ± 0.18 mm and 1.86 ± 0.47 mm FWHM resolution in the X and Y dimensions, respectively. The $12.5 \phi \times 3.5$ mm³ continuous CsI(Na) crystal had a 1.28 ± 0.11 mm and 1.39 ± 0.10 mm FWHM resolution in the X and Y dimensions, respectively. The discrepancy in the X and Y resolutions is most likely due to the hexagonal pattern of the optical fibers, which has a differ-

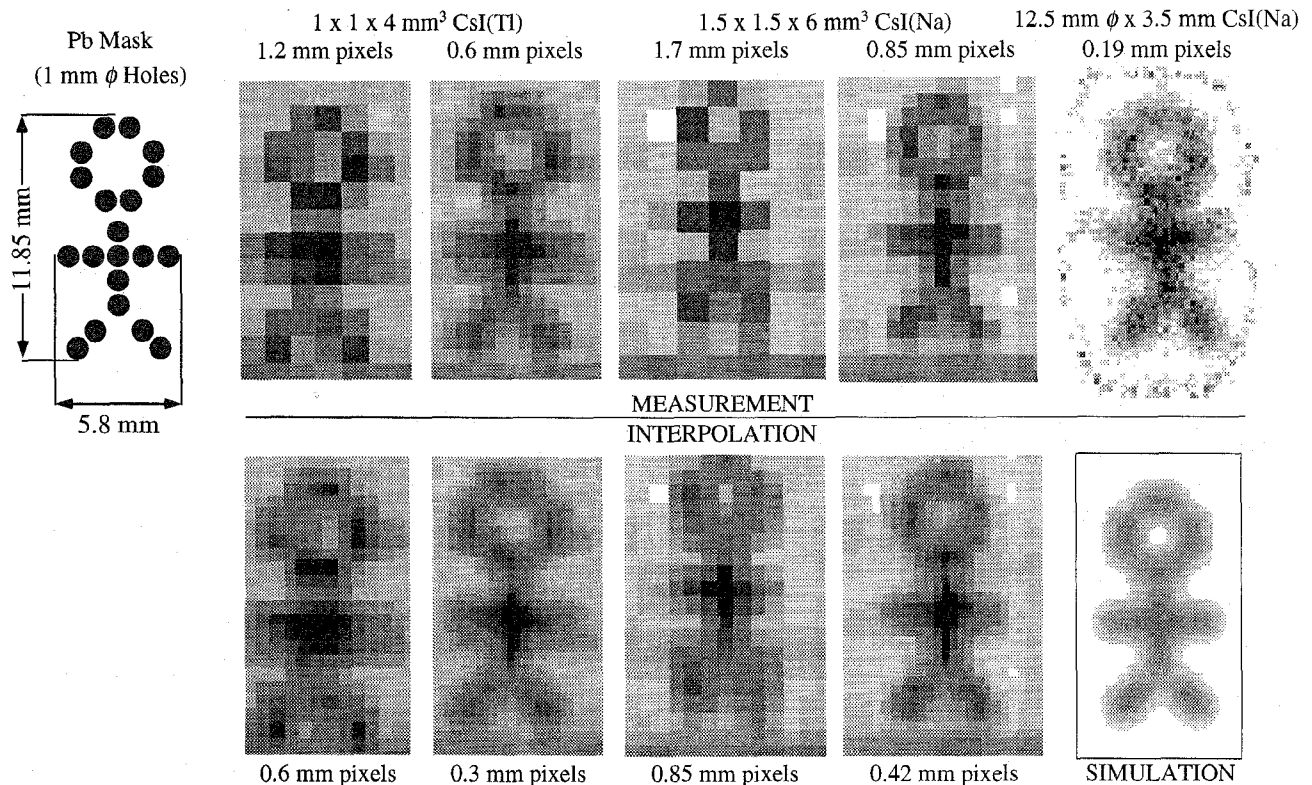


FIGURE 10. Imaging results with various detector arrays of the “stickman” transmission phantom. (Top row) Measured detector results for various sampling schemes and detector arrays. (Bottom row) Digital interpolation of the measured data acts to smooth the resultant image. The simulation (lower, far right) was made with the digital transmission phantom on the upper left.

ent sampling pattern in the X and Y directions. A similar effect was observed with the beta imaging intra-operative probe [9]. The spatial resolution did not improve by the factor of 1.9 that might be expected from the greater pulse height from CsI(Na) crystal (Table 2). This indicates that other factors, such spacing of the fibers and their numerical aperture, may have a dominant effect on the resolution.

V. PRELIMINARY IMAGING MEASUREMENTS

Images were acquired with the 3.5 mm continuous CsI crystals and the $1 \times 1 \times 4 \text{ mm}^3$ CsI(Tl) and $1.5 \times 1.5 \times 6 \text{ mm}^3$ CsI(Na) crystal arrays utilizing light sharing (Fig. 10, top row). The transmission phantom consisted of a “stickman” figure, with 1 mm ϕ holes drilled at ~ 1.2 mm spacing in an 8 mm thick Pb plate. Multiple images were acquired for each detector array and digitally spliced because the phantom did not fit entirely into the detector FOV.

Due to the discrete nature of the two small crystal arrays, the phantom was subsampled by half-pitch offset measurements to minimize pixellation artifacts in the resultant images. The images collected with the discrete arrays were also smoothed by linear interpolation to minimize pixellation in the resultant images (Fig. 10, lower row). For the relatively coarse sampling of these detector arrays, both techniques smooth the final image to make objects appear less pixellated, i.e. smooth the image without increasing spatial sampling. The subsampling also demonstrates the detector integrity and reproducibility for multiple measurements.

The simulated data set (Fig. 10, lower right) was made by 2D Gaussian filtering the digital phantom (Fig. 10, upper left)

with the measured intrinsic resolution of the CsI(Na) continuous detector ($\sigma = 0.57$ mm).

VI. CONCLUSIONS

We have presented encouraging test data on a prototype small area, gamma sensitive detector for intra-operative imaging of residual radiolabeled tumor. The goal of these imaging devices is to guide the surgeon towards high concentrations of activity near the inner surface of the resection cavity. The imaging device utilizes parallel-piped and/or continuous scintillation crystals of high stopping power (CsI(Na), CsI(Tl) and NaI(Tl)) for clinical radioisotopes (e.g. $^{99\text{m}}\text{Tc}$ with 140 keV gamma-rays). The best results were obtained with the CsI(Na) crystals. This was due to their good spectral match to the photocathode, high light output, and good stopping power relative to other detector candidates. Of the three optical coupling implementations, the configuration employing light sharing with crystal arrays was the most versatile and adaptable to existing beta imaging probes.

The poor measured energy resolutions in these devices will preclude effective scatter rejection, especially from deeper sources. However, the gamma imaging probe is intended to be near-sighted, similar to the non-imaging probe in [27], and potentially employ a short collimator. Thus, by viewing proximally located sources, which will contribute fewer scattered events than deeper seated sources, only modest scatter rejection with a lower level threshold is anticipated. One study with non-imaging probes investigated the effects of energy threshold, and determined that higher thresholds, especially for those systems with poor energy resolution,

improved detectability [28]. Probes with very high energy resolution are also under investigation [12] as the trade-offs between near-sighted imaging and poor energy resolution are still unclear.

Ultimately these gamma-ray sensitive imaging detectors will be limited by the collimator. It is not clear how spatial resolution and sensitivity, which are affected by the collimator characteristics, will affect the detection sensitivity of the imaging device. Further measurements and simulations will determine the trade-offs between short, high efficiency collimators and longer, less efficient ones. The gamma sensitive imaging probe may need a larger overall surface area than the beta probe, partly because of the relatively coarse sampling possible with discrete crystals.

This work on fiber-optically coupled imaging probes for *in situ* use has shown its potential as a high resolution imaging device. These devices are capable of imaging beta and gamma distributions in tissue. Now they must be tested in a clinical environment to validate their usefulness in practice.

ACKNOWLEDGMENTS

The authors thank Hilger Analytical and Advanced Detectors for manufacturing the crystal arrays and providing some sample crystals, Drs. Jim Telfer, Barbara Darnell, Jan Iwanczyk, Brad Patt, Yiping Shao and Stefan Siegel for useful discussions, and Richard Koziol for expert technical assistance. This work was funded in part by NIH/NCI grants R01-CA61037, T32-CA09092, DOE contract DE-FC03-87-ER60615, and University of California IRB-0225.

REFERENCES

- [1] PJ Kelly, *et al.* 1987. Imaging-Based Stereotaxic Serial Biopsies in Untreated Intracranial Glial Neoplasms. *J. Neurosurg.* **66**(6):865-874.
- [2] M Ammirati, N Vick, YL Liao, I Ciric, M Mikhael. 1987. Effect of the Extent of Surgical Resection on Survival and Quality of Life in Patients with Supratentorial Glioblastomas and Anaplastic Astrocytomas. *Neurosurgery.* **21**(2):201-206.
- [3] G Baillet, L Albuquerque, Q Chen, M Poisson, J-Y Delattre. 1994. Evaluation of Single-Photon Emission Tomography Imaging of Supratentorial Brain Gliomas with Technetium-99m Sestamibi. *Eur. J. Nucl. Med.* **21**(10):1061-1066.
- [4] LA O'Tuama, *et al.* 1993. Tl-201 Versus Tc-99m-MIBI SPECT in Evaluation of Childhood Brain Tumors: A Within-Subject Comparison. *J. Nucl. Med.* **34**(7):1045-1051.
- [5] J Maublant, *et al.* 1996. Tc-99m-Sestamibi Uptake in Breast Tumor and Associated Lymph Nodes. *J. Nucl. Med.* **37**(6):922-925.
- [6] LR MacDonald, *et al.* 1995. Investigation of the Physical Aspects of Beta Imaging Probes Using Scintillating Fibers and Visible Light Photon Counters. *IEEE Trans. Nucl. Sci.* **NS-42**(4):1351-1357.
- [7] MP Tornai, *et al.* 1995. Development of a Small Area Beta Detecting Probe for Intra-Operative Tumor Imaging. *J. Nucl. Med.* **36**(5):109P.
- [8] LR MacDonald, *et al.* 1995. Small Area, Fiber Coupled Scintillation Camera for Imaging Beta-Ray Distributions Intra-Operatively. *Proc. SPIE: Photoelectronic Detectors, Cameras and Systems.* **2551**:92-101.
- [9] MP Tornai, LR MacDonald, CS Levin, S Siegel, EJ Hoffman. 1996. Design Considerations and Initial Performance of a 1.2 cm² Beta Imaging Intra-Operative Probe. *IEEE Trans. Nucl. Sci.* **NS-43**(4):2326-2335, and references therein.
- [10] EJ Hoffman, MP Tornai, CS Levin, LR MacDonald, S Siegel. 1997. Gamma and Beta Intra-Operative Probes. *Nucl. Instr. Meth.* **A389**:(In Press).
- [11] NE Hartsough, *et al.* 1989. Probes Containing Gamma Radiation Detectors for *In Vivo* Tumor Detection and Imaging. *Proc. SPIE: Catheter-Based Sensing and Imaging Technology.* **1068**:92-99.
- [12] BE Patt, JS Iwanczyk, MP Tornai, CS Levin, EJ Hoffman. 1995. Development of a Mercuric Iodide Detector Array for Medical Imaging Applications. *Nucl. Instr. Meth.* **A366**:173-182.
- [13] F Daghighian, *et al.* 1996. Pharmacokinetics and Dosimetry of I-125-IUdR in the Treatment of Colorectal Cancer Metastatic to Liver. *J. Nucl. Med.* **37**(4):29S-32S.
- [14] Y Shao, SR Cherry, S Siegel, RW Silverman. 1996. A Study of Inter-Crystal Scatter in Small Scintillator Arrays Designed for High Resolution PET Imaging. *IEEE Trans. Nucl. Sci.* **NS-43**(3):1938-1944.
- [15] AJ Bird, T Carter, AJ Dean, D Ramsden, BM Swinyard. 1993. The Optimisation of Small CsI(Tl) Gamma-ray Detectors. *IEEE Trans. Nucl. Sci.* **NS-40**(4):395-399.
- [16] SR Cherry, *et al.* Collection of Scintillation Light from Small BGO Crystals. *IEEE Trans. Nucl. Sci.* **NS-42**(4):1058-1063.
- [17] GF Knoll, TF Knoll, TM Henderson. 1988. Light Collection in Scintillating Detector Composites for Neutron Detection. *IEEE Trans. Nucl. Sci.* **NS-35**(1):872-875.
- [18] CS Levin, LR MacDonald, MP Tornai, EJ Hoffman, J Park. 1996. Optimizing Light Output from Thin Scintillators Used in Beta-Ray Camera for Surgical Use. *IEEE Trans. Nucl. Sci.* **NS-43**(3):2053-2060.
- [19] M Dahlbom, EJ Hoffman. 1988. Evaluation of a Two-Dimensional Array Detector for High Resolution PET. *IEEE Trans. Med. Imag.* **MI-7**:264-272.
- [20] PD Cutler, EJ Hoffman. 1994. Use of Digital Front-End Electronics for Optimization of a Modular PET Detector. *IEEE Trans. Med. Imag.* **MI-13**:408-418.
- [21] S Siegel, SR Cherry, AR Ricci, Y Shao, ME Phelps. 1995. Development of Continuous Detectors for a High Resolution Animal PET System. *IEEE Trans. Nucl. Sci.* **NS-42**(4):1069-1074.
- [22] FD Rollo, Ed. 1977. *Nuclear Medicine Physics, Instrumentation, and Agents.* C.V. Mosby Company. St. Louis. Ch. 6.
- [23] S Siegel, RW Silverman, Y Shao, SR Cherry. 1996. Simple Charge Division Readouts for Imaging Scintillator Arrays Using a Multi-Channel PMT. *IEEE Trans. Nucl. Sci.* **NS-43**(3):1634-1641.
- [24] D Bloyet, J Lepaisant, B Cahan, D Gutknecht. 1992. Charge-Division Multiplexing Circuits for Low Energy Gamma-Ray Detection: Theory and Experimentation. *IEEE Trans. Nucl. Sci.* **NS-39**(2):315-322.
- [25] SR Cherry, MP Tornai, CS Levin, S Siegel, EJ Hoffman. A Comparison of PET Detector Modules Employing Rectangular and Round Photomultiplier Tubes. *IEEE Trans. Nucl. Sci.* **NS-42**(4):1064-1068.
- [26] HH Barrett, W Swindell, Eds. 1981. *Radiological Imaging: The Theory of Image Formation, Detection, & Processing.* Vol. 1. Academic Press. New York. Ch. 5.
- [27] TS Hickernell, HB Barber, HH Barrett, JM Woolfenden. 1988. A Dual-Detector Probe for Surgical Tumor Staging. *J. Nucl. Med.* **29**:1101-1106.
- [28] DP Kwo, HB Barber, HH Barrett, TS Hickernell, JM Woolfenden. 1991. Comparison of NaI(Tl), CdTe, and HgI₂ Surgical Probes: Effect of Scatter Compensation on Probe Performance. *Med. Phys.* **18**(3):382-389.